Robotic Assessment of a Crop's Need for Watering

Amel Dechemi,[†] Dimitris Chatziparaschis,[†] Joshua Chen,[†] Merrick Campbell,[†] Azin Shamshirgaran,[‡]
Caio Mucchiani,[†] Amit Roy-Chowdhury,[†] Stefano Carpin,[‡] and Konstantinos Karydis[†]

I. INTRODUCTION

Agricultural robotics and automation technology play an increasingly critical role across several crop production stages to improve sustainability (e.g., water use optimization). Robotics has been applied for remote and proximal sensing, as well as physical sampling. The procedure of physical sampling and follow-on analysis of plant specimens such as leaves or shoots, which is the focus of this work, often constitutes the only accurate way to measure some essential parameters that affect crop production, such as stem water potential which helps determine a crop's need for watering.

However, both physical sampling and specimen analysis can be quite laborious and often vary among different types of crops. Given the growing agricultural workforce shortages [1], the labor-intensive nature of these measurements poses a severe limitation on how many samples can be collected and analyzed, and restricts how growers and farm consultants can assess local conditions and optimize operations in support of sustainable crop production. This is particularly critical in high-value perennial crops, such as avocados, citrus, almonds, nuts, and vines. Hence, robotics and automation technology can be employed to support physical sampling and specimen analysis.

The goal of this work is to develop robotics and automation technology tools that can help assess watering needs for tree crops. The primary focus lies in automating the process of measuring stem water potential (SWP). SWP is a metric frequently used by agronomists and growers to optimize irrigation schedules for crops [5], with the intent of reducing water waste and maximizing profits [15,19]. The current industry standard for obtaining SWP measurements is the Scholander pressure chamber method [16], which involves the insertion of a leaf sample into a pressure chamber with its stem's excised end exposed (Fig. 1(a)). After the sample is secured, a human operator slowly activates a valve to pressurize the chamber while also observing the water expression at the end of the exposed stem through a magnifying glass (Fig. 1(b)). The pressure necessary to force water out of the stem determines the SWP. The process measures the capacity of the cells to retain water by pressurizing the leaf. The less free water there is in the plant, the greater the pressure required to cause the leaf to exude water. When taken in pre-dawn conditions (i.e. performed before sunrise) and plant stomata are closed, the measurement is at equilibrium with soil moisture conditions. Subsequent measurements can then precisely determine water deficit, and thus irrigation demand to meet evapotranspiration loss. A precise measurement of the SWP is essential to assess the water deficit of the plant and to therefore adjust irrigation. Given that 80% of managed freshwater in the US is consumed by agriculture [21] and that evapotranspiration model estimates widely diverge [8], even modest improvements in irrigation practices can have huge impacts, especially in the semi-arid southwestern US that periodically undergoes drought periods while providing a large fraction of fruits and vegetables.

Considering the aforementioned labor-intensive steps in measuring SWP using the pressure chamber method, but recognizing its significance in crop production, some alternative methods have been proposed. Some rely on remote sensing using spectral reflectance or multi-spectral imaging to determine water potential [20,25]. Their greatest values are their non-invasive characteristic, much like the pressure chamber method, and scalability since these methods are intended as a faster alternative to the pressure chamber for mass assessment. Though initially promising, these methods are highly sensitive to an intractable external factor, i.e. light variability due to weather and solar motion. Zhao et al. [25] mounted multispectral cameras on a small UAV to take high-resolution multispectral images of orchards for SWP prediction using the canopy Normalized Difference Vegetation Index (NDVI), but mentioned the high variability in data collected from different flights within the same day due to solar motion. Vila et al. [20] used remote sensors and spectral reflectance as a proxy for SWP measurements but had a low correlation coefficient and thus concluded this method cannot serve as a replacement for the pressure chamber method. Since the concepts of spectral reflectance and imaging may not be mature yet for this application, our work seeks to directly automate the pressure chamber method for assessing SWP.

Specifically, we are developing a robotic system that can physically collect and analyze plant specimens in the field at scale to determine the SWP, thus removing some of the main practical obstacles to the implementation of precision agriculture, and providing growers and farm consultants with granular data currently not available. The overall system developed in this work aims to automate time-consuming and difficult to perform tasks, namely collecting multiple leaves from tree crops and automating some parts of the follow-

---

[†] Dept. of Electrical and Computer Eng., Univ. of California, Riverside, 900 University Avenue, Riverside, CA 92521, USA. Email: {adech003, dchat013, jchen142, mcamp077, caiocesr, roychowdhury, karydis}@ucr.edu.

[‡] Dept. of Computer Science and Eng., Univ. of California, Merced, 5200 N Lake Rd, Merced, CA 95343, USA. Email: {ashamshirgaran, scarpin}@ucmerced.edu.

We gratefully acknowledge the support of USDA-NIFA under grants # 2021-67022-33452 and # 2021-67022-33453 and The University of California under grant UC-MRPI M21PR3417. Any opinions, findings, and conclusions or recommendations expressed in this material are those of the authors and do not necessarily reflect the views of the funding agencies.

(a) (b) (c)

Fig. 1: (a) Working principle of the pressure chamber. (b) Manual visual inspection is currently performed in the field for SWP analysis. (c) Illustration of the concept proposed in this work. A mobile robot autonomously selects multiple measurement locations for sample collection and retrieves leaves. These are later on conveyed to a human operator who uses a pressure chamber retrofitted with our machine-vision-assisted technology to determine the pressure defining the SWP.

on SWP analysis. With reference to Fig. 1(c) which outlines the overall idea, our system first determines the location of trees in the field to sample leaves from (Section II). This part contributes to informed path planning under motion energy constraints for autonomous mobile robots. Once sentinel trees have been selected, a mobile manipulator with a custom-designed end-effector is tasked to autonomously retrieve leaf samples and transport them back to a SWP analysis station (Section III). Our work here contributes key information regarding component selection, system design, and system integration features underlying autonomous perception-actuation loops for mobile manipulation. When the robot has reached the SWP analysis station, a human operator loads the samples into a machine-vision-assisted pressure chamber to determine the exposed leaf stem's wetness (Section IV). This last part contributes data and methodologies to employ machine vision and machine learning to help automate the very labor-intensive process of determining the point of xylem water expression during SWP. In the remainder of the manuscript, we detail the aforementioned process and contributions. Finally, we summarize lessons learned and sketch ideas for future research enabled by the work described herein (Section V).

II. INFORMED PLANNING FOR SELECTION OF SAMPLING TREE LOCATIONS

The overall process initiates by determining a sequence of trees to collect leaf samples from. A direct, brute-force approach would be to sequentially sample from all trees in the field. However, such a process would not scale with commercial field sizes. To make this process tractable, growers currently rely on sampling from a small number of so called *sentinel trees*. When measurements are taken manually, a small fixed set of sentinel trees are preselected and sampled throughout the growing season. A drawback of this approach is that samples from a small number of trees are used to extrapolate the values of relevant parameters over significantly larger areas, a process which may yield inaccurate results and hence lead to sub-optimal watering decisions.

Deployment of one [10] or more [9] autonomous mobile robots in the field to collect samples opens up the possibility of considering a larger set of sentinel trees, and also to plan a sequence of sampling locations on the fly, ideally based on the outcome of former measurements. This process is subject to an energy constraint, i.e. the motion planning algorithm that determines the next tree for sample collection has to ensure that the robot will not run out of energy before returning to a preassigned location, where its battery can be either recharged or swapped for a new one. With this approach, a much larger set of potential sentinel trees can be considered, and the planner task is to select at run time the most suitable subset for sampling. While in previous precision agriculture works we studied this problem as an instance of the orienteering problem [11], we here cast it as an instance of the informed path planning problem (IPP) where the goal is to solve the following optimization problem:

$$p^* = \arg\max_{p\in\Pi} f(p) \qquad \text{s.t. } C(p) \leq B \ .$$

Here, Π is the set of all paths through the set of sentinel trees, $f(p)$ is the *quality* of the path, and $C(p)$ is the cost of the path that is bounded by the available energy budget B. Ideally, the quality of a path $f(p)$ would be assessed by the root mean squared (RMS) error of the scalar field being estimated. Because in practice the ground truth is unknown, RMS cannot be directly computed, and we rather aim at collecting samples that reduce this metric. To this end, we use Gaussian Processes (GPs) to model the underlying scalar parameter being estimated, i.e. SWP [17]. GPs are an appealing modeling approach because of their efficient posterior update, and they are also widely used in geostatistics to model physical phenomena (where the approach is usually referred to as *kriging*.) Specifically, we use a Matérn kernel with smoothness $\nu = 1.5$ as this has proven to be an appropriate choice in agricultural applications.

Using GPs, after each sample is collected we can update the uncertainty associated with the scalar field being estimated, and then iteratively build a path collecting more samples at sentinel trees located in regions with high uncertainty. Therefore, after each sample is collected the importance of each sentinel tree is reassessed based on the values collected up to that point. Note that in our approach samples are collected only at the selected sentinel trees, and not along the way. This differs from our previous work [11] where each candidate sampling location's value was predetermined and fixed. Different metrics can be used to estimate the value of collecting a sample at a given location. In some instances the variance of the GP estimate is used [2], with the goal of collecting samples in high variance regions to reduce uncertainty. In our work we are currently focusing on *mutual information* (MI). Let $\mathcal{S}$ be the set of sentinel trees, and $\mathcal{A} \subset \mathcal{S}$ a subset of already sampled sentinel trees. The mutual information between these two sets is defined as

$$MI(\mathcal{A};\mathcal{V}\setminus\mathcal{A}) = H(\mathcal{V}\setminus\mathcal{A}) - H(\mathcal{V}\setminus\mathcal{A}|\mathcal{A}) \ ,$$

where H is the entropy associated with the given sets, based on the current estimate. Owing to the fact that GPs are used for the underlying estimates, closed-form expressions can be be obtained for MI [17]. Then, the path p can be iteratively extended by adding the sentinel tree

$$t = \arg\max_{t\in\mathcal{V}\setminus\mathcal{A}} \left[H(\mathcal{V}_t\setminus\mathcal{A}_t) - H(\mathcal{V}_t\setminus\mathcal{A}_t|\mathcal{A}_t)\right]$$

where $\mathcal{V}_t = \mathcal{V} \setminus \{t\}$ and $\mathcal{A}_t = \mathcal{A} \cup \{t\}$ subject to the constraint that after having reached the tree being added to the path there must be enough energy left to reach the final destination, i.e. the location where the pressure chamber is located. Once a new sampling point is selected, a path to it is computed using the rapidly-exploring random tree (RRT) motion planning algorithm informed by the fixed locations of the trees in the orchard. This process is iterated until the end point is selected and reached.

To test the viability of this approach, we performed extensive tests in a simulated environment, where under controlled conditions we varied the underlying scalar field being estimated, as well as the number of sentinel trees. Figure 2 displays a subset of our obtained results, and shows that the proposed approach is capable of reconstructing the underlying field even with a small budget by visiting the most significant (i.e. informative) locations. Figure 2(c) also displays the path produced by the planner. (The path in Fig. 2(e) is omitted for figure clarity.) Additionally, deployment of the developed strategy for determining sampling locations during actual field experiments is presented in the following section.

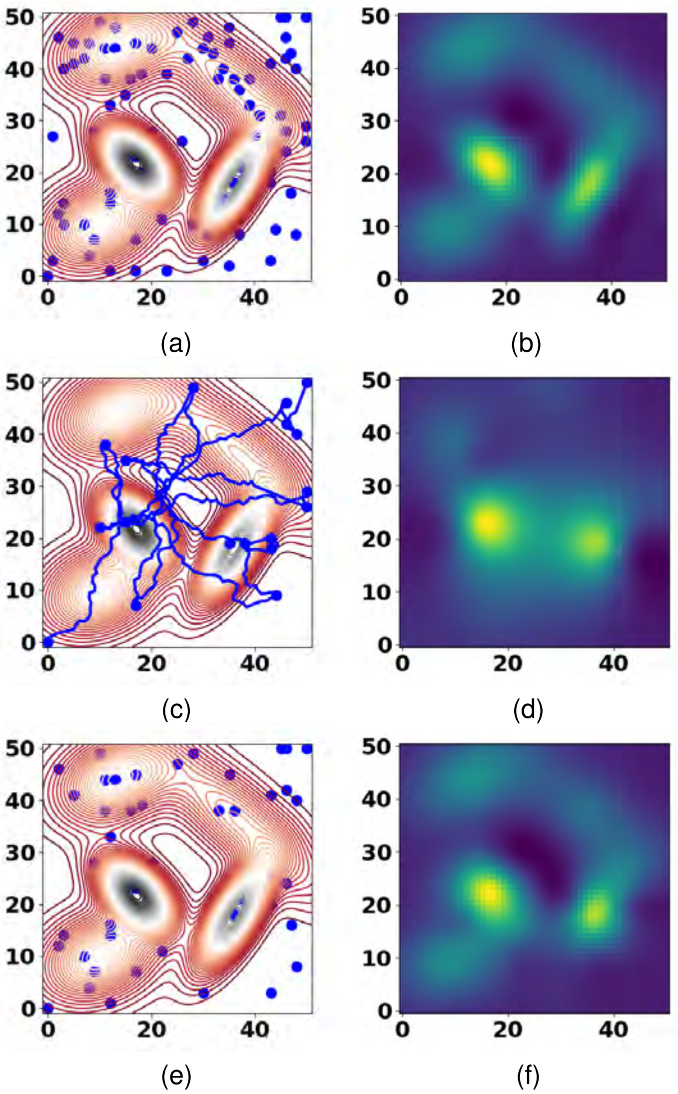

(a) (b)

(c) (d)

(e) (f)

Fig. 2: (a) Underlying scalar field (ground truth) and the location of 100 candidate sentinel tree locations; (b) GP reconstruction obtained if the robot is allowed to collect samples at all locations (used for benchmarking purposes). (c) Sampling points and path selected by the algorithm with a budget C of 750 (small value) and (d) reconstructed scalar field obtained using these sampling locations. (e) Sampling points (path not shown for image clarity) selected by the algorithm with a budget C of 2000 (average value) and (f) reconstructed scalar field obtained using the latter locations. In the simulation, distances and budgets are in meters.

III. ROBOT DESIGN AND DEPLOYMENT FOR AUTONOMOUS LEAF RETRIEVAL

Once a desired sequence of sentinel trees has been selected, the deployed robot (a wheeled mobile manipulator–see Fig. 3) needs to navigate toward the corresponding field locations to physically sample leaves. We can perform this process autonomously by integrating four core functionalities: 1) end-effector design to cleanly cut and retain leaves; 2) on-board visual perception to detect and localize candidate leaves; 3) robot arm manipulation to enclose a candidate leaf with the end-effector and cut it; and 4) waypoint navigation of the wheeled mobile robot based in the field to travel from one sampling location to another and back to the SWP analysis station. Our previous work [3] has focused on studying the third functionality, namely co-optimizing perception and ac-

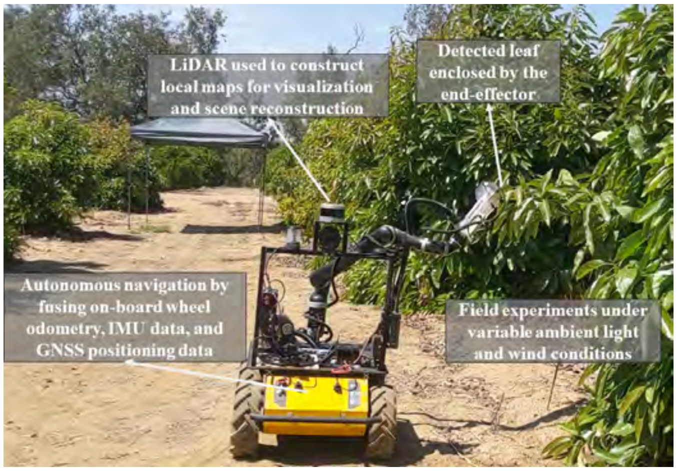

Fig. 3: The agricultural robot used in this work for robotic assessment of a crop's need for watering.

tuation for autonomous leaf retrieval in static cases. Herein we present research findings on the important components of the development and assessment of the end-effector, camera selection and assessment to enable visual leaf identification and pose estimation, and overall system integration and field deployment and testing. We anticipate that the information included herein can also help other researchers working on related topics of robotic visually-informed physical sampling.

A. *End-effector Design*

To be appropriate for SWP analysis, the end-effector needs to cleanly cut the leaf stem to separate the test specimen from the host tree, as well as retain the cut leaf for the subsequent pressure chamber analysis since a damaged specimen can negatively impact the analysis.

1) **Requirements and Benchmark Testing for Efficient Cutting***:* Given the radius of a leaf stem (r), we can calculate the required cutting force as $F = \pi r^2 \tau$, with shear stress $\tau \in [0.85, 5.90]$ MPa for cutting organic plant matter [24]. We measured the diameter of 10 leaves from four different tree crops (avocado, clementine, grapefruit, and lemon) for a total of 40 leaves. The average leaf stem diameter was 2.09 mm with a standard deviation of 0.51 mm. With this information, we were able to estimate that the force required to cut the average leaf ranged from 2.9 to 20 N. However, organic matter such as leaf stems exhibit visco-elastic properties. When stress is applied, the material resists the deformation linearly with time. When stress is removed from an elastic material, the material returns to the original non-deformed state. Based on visco-elastic material principles, faster cuts will require less force and result in less deformation of the leaf stem. Hence, the rate of cut is equally important to the delivered force. For this reason, we conducted a set of cutting experiments to determine the optimal cutting rate.

Specifically, an initial prototype leaf cutter was placed on a level platform above a measuring stick with a high-speed camera positioned to face the cutting blades. Three distinct gear sets were 3D-printed so that they could be inserted between the servo motor and the cutting mechanism to adjust the speed. For each gear ratio (7:13, 22:13, 41:13), four leaves were inserted into the mechanism and the high-speed camera recorded the cutting attempt for each leaf. The selected motor had sufficient torque margins so that the desired cutting force could be delivered with all tested gearing setups. Recorded frames were analyzed to determine the terminal speed of the cutting mechanism. With known camera frame rate (240 fps) and travel distance (19.1 mm), the cutting speed of the mechanism can be determined as

$$V = \frac{\delta x}{\delta t} \approx \frac{\Delta x}{\text{frame rate} \times \text{frame count}} \enspace .$$

TABLE I: Leaf Cutting Velocity Tests

Gear Ratio	Frame Count	Time (s)	Speed (m/s)	Success
7:13	48	0.200	0.095	No
7:13	40	0.167	0.114	No
7:13	39	0.163	0.117	No
7:13	41	0.171	0.112	No
22:13	20	0.083	0.229	No
22:13	25	0.104	0.183	No
22:13	17	0.071	0.269	No
22:13	18	0.075	0.254	No
41:13	16	0.067	0.286	Yes
41:13	20	0.083	0.229	Yes
41:13	11	0.046	0.416	Yes
41:13	14	0.058	0.327	Yes

Of the three gear ratios, only the fastest gearing resulted in a cleanly cut leaf. Table I shows results from all trials. From this analysis, we determined that the minimum cutting speed for the cutter should be 0.312 m/s. With both the cutting force and rate determined, we proceeded to develop an end-effector with a desired target force of 20 N at 1.1 m/s. This rate provides sufficient margin over the empirically determined minimum cutting speed of 0.312 m/s to account for any losses and work with a wide variety of tree leaves.

2) **Prototype End-effector Assembly***:* The cutting mechanism utilizes two four-bar linkages to actuate a set of sliding gates, one of which contains a razor blade to cleanly sever the stem without damaging the leaf (Fig. 4). The gates also help retain the leaf within the end-effector's chamber after removal from the tree. These four-bar mechanisms are connected via a geartrain to achieve synchronized motion. A low-cost, high-torque R/C servo (FEETECH FT5335M) drives the geartrain while being amenable to adequate position control. The end-effector's chamber has an opening of 110 mm × 45 mm and a depth of 185 mm to accommodate for typical avocado leaves (which are the largest of the four tree crops considered in this work). The end-effector is constructed with miniature aluminum extrusions, lightweight 3D printed parts, and laser-cut acrylic panels. The assembly weighs a total of 1.09 kg, which is 42% of the robotic arm's 2.6 kg payload we used to integrate our end-effector onto (Kinova Jaco 6-DoF).

The end-effector was designed to operate symbiotically with the Robot Operating System (ROS). High-level control commands can be handled via a ROS node. The node receives commands from published ROS topics and issues commands to the end-effector via Serial UART communication. The end-effector contains an embedded microcontroller (Arduino Due) to parse the received serial commands and control the motor

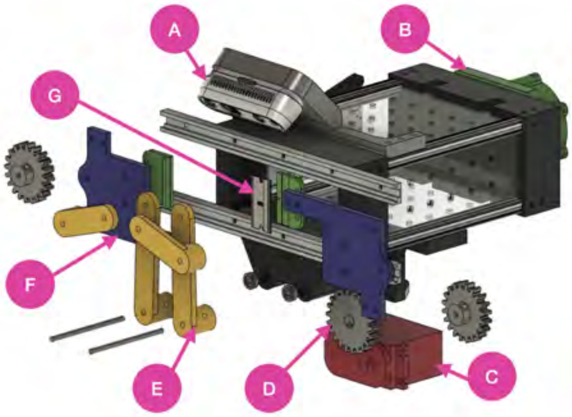

Fig. 4: Exploded view of the end-effector. Key components of the assembly include an Intel RealSense D435i Depth Camera (A) and an interchangeable robotic arm mount (B). The FEETECH FT5335M R/C servo (C) is connected via a geartrain (D) to four-bar linkages (E). This mechanism closes the gates (F) to cut the leaf with the razor blade (G). This separates the leaf from the tree and retains it within the enclosure for subsequent SWP analysis.

that drives the cutting mechanism. A breakout board connected to the Arduino contains a "safe/armed" switch along with LED indicators to reduce the risk of accidental injury from the razor blade (for redundancy, the high-level ROS control node also has a software "safe/armed" switch). A 7.4 V 2S LiPo battery powers the assembly. The overall prototype was mounted on top of a commercial mobile manipulator (Clearpath Husky wheeled robot with Kinova Jaco robot arm) also running ROS.

B. On-board Perception

Our work considers an "eye-on-hand" configuration whereby a camera mounted on top of the end-effector (Fig. 4) is used to provide information regarding leaves to sample as well as their position and orientation (pose) in 3D space.

1) **Camera Selection & Placement Evaluation***:* Several cameras were considered as the sensing modality for the proposed end-effector (Table II). Although the ZED and ZED2 have solid performance, they were excluded because of their wide baselines which do not fit our intended eye-on-hand configuration. We evaluated the performance of the three other cameras in different conditions including indoor and outdoor environments. The obtained results show that the Realsense (RS) D435i has the best performance, especially outdoors where it is able to provide a viable depth image at close ranges. Furthermore, we were able to obtain high-quality point clouds at depth ranges lower than those provided in manufacturer specifications (0.1 m). Sample images collected using the RS D435i are shown in Fig. 5.

Two eye-on-hand configurations were considered, one looking straight ahead and one looking downward at a 45° angle. While the former case can lead to longer look-ahead distances, the latter one was ultimately selected. This configuration balances between providing useful depth information about the tree (needed for obstacle avoidance and navigation around tree branches) and allowing for leaf detection and localization (needed for aligning the end-effector with the leaf to cut it).

TABLE II: Candidate Cameras Specifications

Camera	Baseline (mm)	Depth Range (m)	Field of View
ZED	120	0.3 – 25	90° x 60° x 100°
ZED2	120	0.3 – 20	110° x 70° x 120°
ZED mini	63	0.1 – 15	90° x 60° x 100°
RS D435i	50	0.2 – 3	87° x 58° x 95°
RS D455	95	0.4 – 6	87° x 58° x 95°

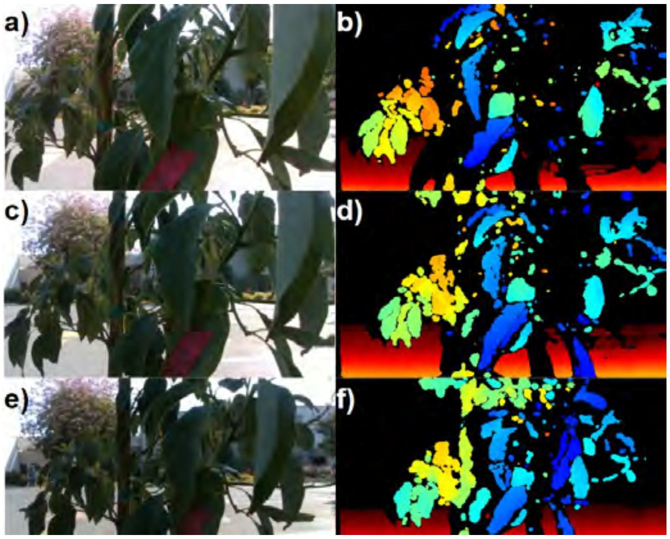

Fig. 5: Sample RGB and depth images collected from RS D435i in an outdoor environment at (a)–(b) 15 cm, (c)–(d) 20 cm, and (e)–(f) 25 cm.

2) **Scene Understanding***:* The on-board camera yields a 3D point cloud which we are consequently using to detect and localize appropriate leaf candidates via 3D bounding boxes. The process is visually exemplified in Fig. 6 and described next. First, we removed outliers caused by noise in sensor measurements and segment out the background. The degrees of outlier detection and background removal depend on user-tuned hyperparameters. Then, we applied downsampling for computational expediency without loss of performance. Next, we grouped the remaining point cloud segments into clusters using the Density Based Spatial Clustering of Applications with Noise (DBSCAN) approach. DBSCAN relies on two key parameters, the minimum distance between two points to be neighbors (*eps*) and the number of minimum points to form a cluster (*MinPoints*). Each resulting cluster is considered a potential leaf and described by a 3D bounding box defined by center $C = [c_x, c_y, c_z]^T$, dimensions $D = [h, w, d]$, and orientation $R(\theta, \Phi, \alpha)$. Then, we filtered the clusters using geometric features of the bounding box: number of points, volume, and leaf ratio. Finally, the pose of the center of each bounding box was set as the 6D pose of a leaf candidate.

To validate our approach, ROSbags were collected both in indoor (lab with constant light conditions) and outdoor (local orchard with varying light conditions) settings. In indoor experiments, the robot arm with the camera was placed at different distances $(0.2 - 0.3$ m) from a potted tree, whereas outdoor data were manually collected over a wide range $(0.5-1.6$ m) of distances from trees. A total of 25 point clouds

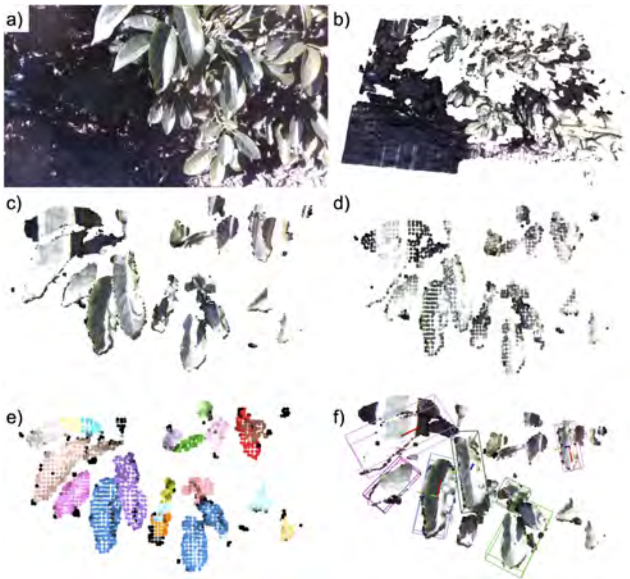

Fig. 6: Key steps in our proposed leaf detection and localization process. The sample here corresponds to an outdoor point cloud: (a) corresponding RGB image of the tree, (b) raw point cloud, (c) background removal, (d) downsampled point cloud, (e) segmented clusters, and (f) detected candidate leaves without 6D pose bounding boxes. (Image taken from [3].)

were collected (10 indoor and 15 outdoor) and tested offline with different combinations for *eps* and *MinPoints* parameters, to determine appropriate values.

Results demonstrated detection 80.0% on average (maximum: 90%) in the indoor dataset and detection 79.8% on average (maximum: 85%) outdoors (see Table III). Further, we observed that the distance between the camera and the tree affects parameter selection for point cloud processing. As the distance increases, values for *eps* and *MinPoints* should increase and decrease, respectively.

TABLE III: Leaf Point Cloud Detection

	Point Clouds	Total # Leaves	Average Detection	Percentage
Indoor	10	20	16	80.0%
Outdoor	15	99	79	79.8%

C. Evaluation of Autonomous Leaf Extraction Efficacy in Controlled Settings

The system operation flow diagram regarding how to detect and extract a leaf from a tree is depicted in Fig. 7. First, the robot base needs to be in close proximity to a tree to sample leaves from.[1] Once in place, obtained point cloud data from the camera mounted on the end-effector are processed in real-time using Open3D [26] running on an Intel i7-10710U CPU, without any additional GPU acceleration. Identified and segmented leaves serve as target for the arm to move and align the end-effector along a detected leaf candidate within the end-effector's workspace, at an offset position from the center of the leaf. The offset distance can be selected in relation to the length of the leaf. When the end-effector reaches the target offset, the arm is commanded to move along a linear path toward the leaf. When the leaf is enclosed, the end-effector cuts the leaf and retains it. Then, the arm returns home, and the process may repeat as part of a larger field sampling procedure; see next subsection.

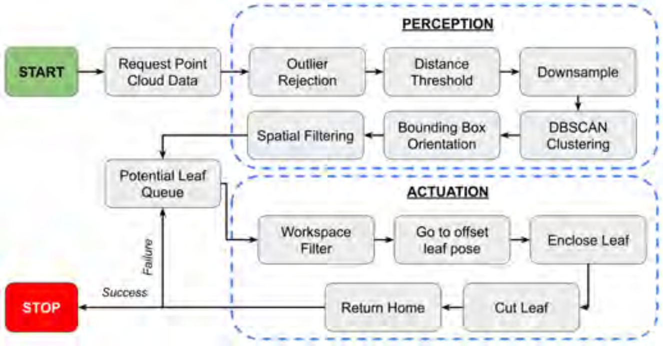

Fig. 7: Our approach for autonomous leaf extraction integrates perception and actuation. Point cloud data are processed at runtime to segment leaves and add leaf candidates into a queue. Candidate leaves are then passed to the robot arm and end-effector. If a cut is successful, the routine ends but if not, the next leaf in the queue is requested and the process repeats.

We evaluated our developed autonomous leaf extraction pipeline in controlled settings indoors, with a real potted avocado tree. The end-effector was initialized at random poses near the base of the tree at distances ranging between $0.2-0.3$ m from the edge of the tree canopy. An experimental trial consisted of collecting a point cloud, storing the identified and localized potential leaves in a queue, and then sending the queued leaves to the arm for a retrieval attempt. Each trial concluded once the queue was depleted and the tree was repositioned for the next trial. Figure 8 outlines this process. Out of 46 trials, 63 potential leaves were detected by the point cloud.[2] After filtering the potential leaves to remove the leaves outside of the work space, 39 viable leaves remained. Out of these leaves, 27 were captured successfully (69.2%) while 21 of the 27 captured leaves were cut (77.8%). The mean point cloud processing (perception) time was 5.6 sec and the mean cutting (actuation) time was 10.6 sec. The mean total retrieval time was 16.2 sec. These findings demonstrate that the developed system can successfully cut and retain leaves in controlled settings.

---

[1] In detail, the mobile base needs to be at an offset distance from the tree canopy so that the intersection of the reachable workspace of the robot arm and the outer canopy is maximized. Note that considering the leaf and end-effector 3D orientations is crucial, hence the robot should also avoid being too close to the canopy as this can lead to singular configurations for the arm. This trade-off is captured in our work via the notion of *viable leaves*. These are leaves that are detected, within the reachable workspace of the robot, and away (in a topological sense) from singular configurations that could bring the robot arm to a locked status.

[2] Note that each point cloud in the trial may produce a variable amount of leaves, hence the higher number of potential leaves than trials.

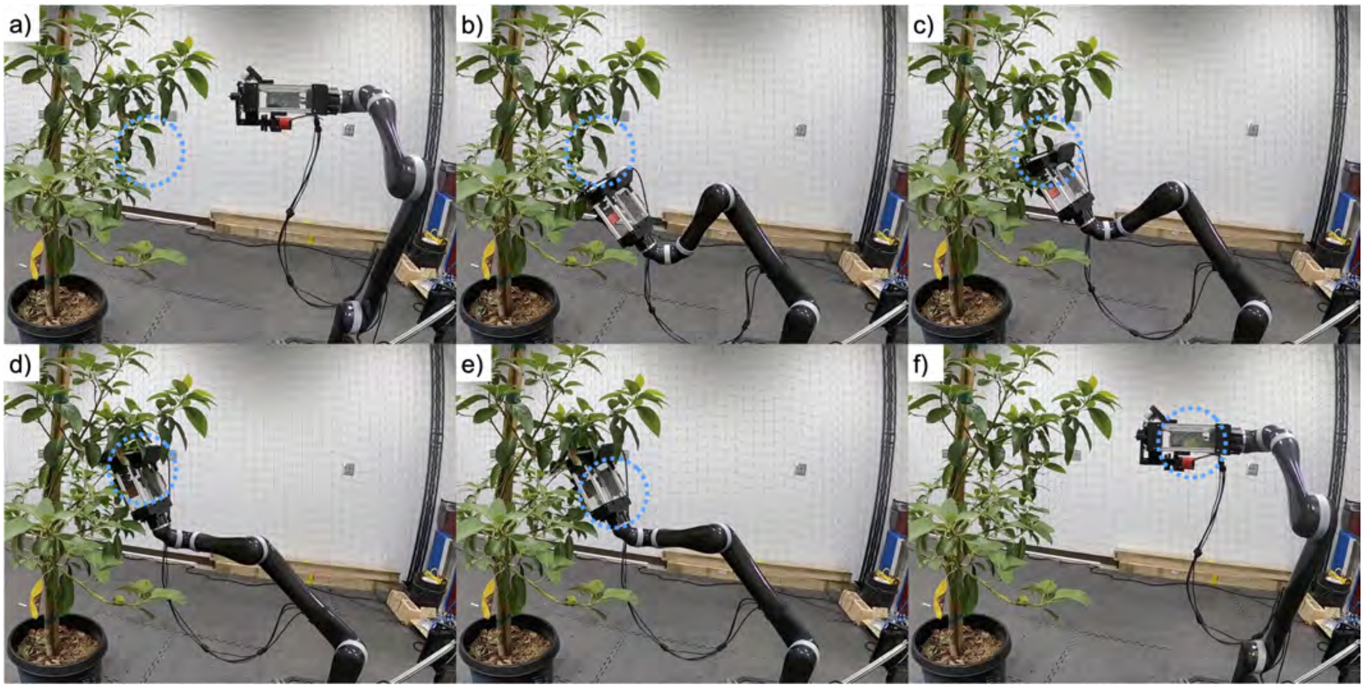

Fig. 8: Sample leaf retrieval process. (a) Point cloud data are processed to determine a potential leaf. (b) Given a detected leaf within the workspace, the arm will move to an offset position. (c) The arm moves in a linear motion toward the leaf to enclose it. (d-e) When in place, the end-effector will cut the leaf and retain it into the enclosed chamber. (f) After completing the cut, the arm will return to the home position. (Image taken from [3].)

D. Overall System Integration and Field Experiments

The final step toward enabling autonomous leaf retrieval comprises the integration of waypoint navigation and deployment in real-world field experiments. To assess the robustness of our framework, consider a list of sentinel tree locations. This information is used to create desired waypoints that serve as the locations the robot should visit and attempt to sample leaves from the corresponding sentinel trees. Then, we integrate the leaf extraction steps outlined in Fig. 7 for every encountered tree. When the leaf extraction process terminates for each sentinel tree, the robot moves to the next sampling area and the process repeats, or returns to the analysis station where collected leaves are retrieved by the human co-worker and placed into the pressure chamber for automated stem water potential analysis (see Section IV that follows).

Field experiments were conducted in an avocado tree field at the Agricultural Experimental Station (AES; $33^\circ\ 58'\ 3.2592''\ N,\ 117^\circ 20'\ 7.0296'' W)$ at the University of California, Riverside. We use satellite imagery to construct an outline of the geometry of the field, including tree positions. As an example demonstrating how to reduce the general planner to practice, we consider the case of sampling from three sentinel trees within an area of interest measuring $11 \times 6\ m^2$. Selected sentinel trees and the underlying GP reconstruction are shown in Fig. 9. The computed path for the robot to follow as per our planning algorithm in Section II is also highlighted in the figure.

The satellite-based map is described in the World Geodetic System 1984 (WGS-84), but to be usable from the robot it needs to be linked with the mobile robot's local map which is in turn used for robot navigation. We use the Universal Transverse Mercator (UTM) projection to express the satellite-based sampling points into desired waypoints in the robot's local coordinate system. The mobile robot base we use (Clearpath Husky) can obtain odometry information from its wheel encoders, orientation, linear velocity and angular acceleration measurements from its embedded inertial measurement unit (IMU) module, and positioning data captured by its onboard Global Navigation Satellite System (GNSS) receiver. This information is used onboard and in real time by the $navsat\_transform\_node$[3] from the built-in ROS navigation stack, to broadcast the pose (i.e. position and orientation) of the mobile robot base in the UTM local coordinate system. The robot's pose is updated in the local frame while moving, by using fused information from the three onboard sensory modules. The movement actions in the local frame are handled by the $move\_base$ [4] ROS package, which generates velocity commands for the mobile platform in order to acquire the desired pose in the local frame. For additional safety, our developed system allows a human operator/supervisor to trigger when the robot switches between navigation and leaf-picking modes, as well as to skip a sampling location and move to the next one. The robot arm is rigidly affixed to the mobile base; coordinate transforms between the mobile base and each arm link frame as well the end-effector frame are all readily computed via closed-form forward kinematics expressions.

In our experiments, the mobile robot starts from a known position on the map. The robot arm is initialized turned toward the right-hand side of the mobile base, so that the camera

---

[3] http://docs.ros.org/en/jade/api/robot_localization/html/navsat_transform_node.html

[4] http://wiki.ros.org/move_base

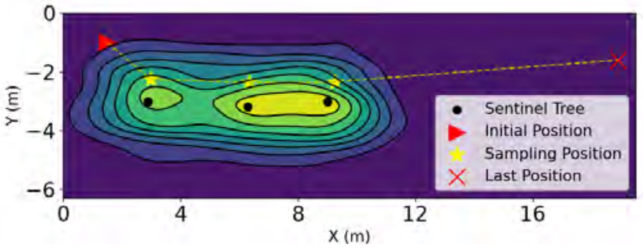

Fig. 9: GP reconstruction of the avocado field with three sentinel trees considered during field experiments.

mounted on the end-effector has an unobtrusive view to the tree canopies from the right-hand side of the robot as the latter moves forward.[5] The first desired pose is transmitted to the platform, which in turn moves toward the target tree at the desired position using the generated trajectory. As the first goal pose is reached, the mobile platform stops and the leaf retrieval process subsequently initiates. The perception module processes the collected point cloud and returns the center and dimensions of each candidate leaf with respect to the camera frame. The tip and stem positions are then estimated with respect to the end-effector's frame, and the manipulation planning procedure outlined in Fig. 7 is executed. Figure 10(a) illustrates an instance of the mobile robot when sampling at the third desired location. Three candidates leaves have been successfully detected, and the process can then proceed to the actuation procedure. Figure 10(b) depicts the path followed by the robot in the field experiment until reaching the third sentinel tree. The complete field experiment can be viewed in the supplemental video at https://youtu.be/xu4zrTe_S-U.

IV. MACHINE-VISION-ASSISTED IDENTIFICATION OF LEAF STEM WETNESS IN SWP ANALYSIS

The final stage of this work concerns the automated identification of leaf stem wetness during stem water potential (SWP) analysis. We consider that leaves have been collected by the mobile manipulator and transported back to the SWP analysis station. There, a human operator loads/unloads a leaf into the pressure chamber. The latter, is retrofitted with both additional hardware as well as machine-vision software to enable automated visual identification of the status of the leaf xylem (dry/wet). Our approach provides live feed of the stem as the pressure in the chamber increases. When the status changes from dry to wet, our developed system identifies the transition and alerts the operator so that they can note down the pressure. To accommodate for the large variability that is typically present in this process, our proposed solution hinges on learning-based machine vision. In the following we detail the data acquisition, hardware and software development, and algorithm training and evaluation components that are necessary to automate this labor-intensive process of determining the leaf xylem wetness status.

A key part of our work is the creation of a new stem image dataset, collected over the course of two sessions (a two-week long in July 2022 and another one-week long in June 2023) at UCR AES fields in an arid hot climate. We collected upwards of 80 avocado and orange leaf samples (for system training and validation) and 20 lemon and grapefruit leaf samples (for preliminary evaluation of the developed method's generalization capacity), performed conventional stem water potential (SWP) analysis while video recording each session, and extracted frames from the recordings to build the dataset.

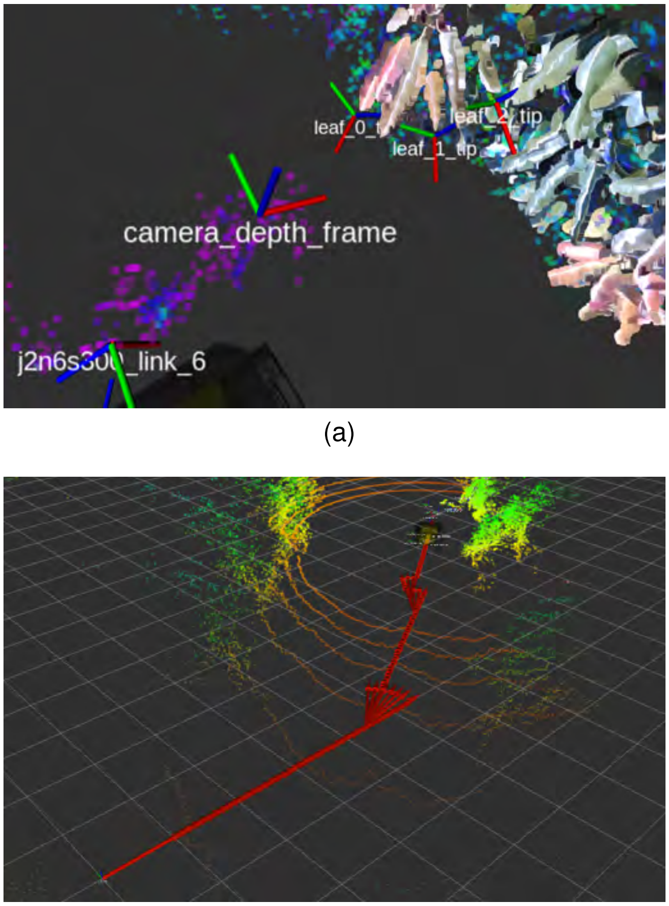

(a)

(b)

Fig. 10: (a) Visualization (in ROS RViz) of the mobile robot at the third sentinel tree location. Each depicted coordinate system represents the corresponding state at the captured moment. Three leaf candidates, namely $leaf\_\{0,1,2\}\_tip$, have been detected. Given these candidates, the actuation module will decide to reach the closest one and attempt to cut and retain. (b) Visualization of the path followed in the avocado experimental field. The captured moment shows the robot in the third leaf sampling position, while at the leaf detection procedure. Red arrows illustrate the odometry poses along its path from the starting position to the sampling position.

A. Data Acquisition

1) **Setup and Procedures:** We considered two pressure chamber setups, the Pump-up and 600D models from PMS Instruments. The former is powered manually by performing alternating upward and downward strokes that increase the

---

[5] This configuration helps distribute the load to the mobile base as evenly as possible given other embedded parts, and minimizes occlusions to an embedded LiDAR sensor that is currently used to collect data during operation to create the visualizations shown in Fig. 10).

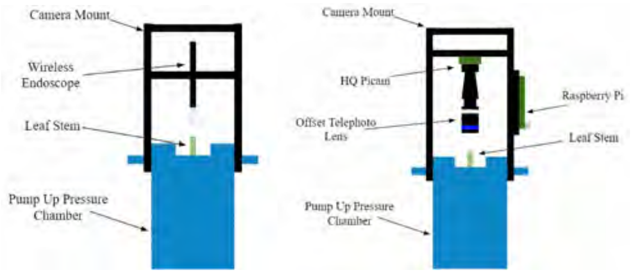

Fig. 11: Diagram showing how the custom-made mount and camera setups (left: endoscope, right: high quality Picamera) are mounted onto the manual pump-up chamber. The mounting onto the 600D nitrogen gas pressure chamber follows a very similar manner and is not shown here for brevity.

pressure inside the chamber (similarly to a hand pump). The latter uses compressed nitrogen gas which enters the chamber by rotating a knob connected to a valve.[6]

We also considered two different miniature cameras to be mounted onto the chambers. These included a high quality miniature camera (HQ Picamera) together with a Raspberry Pi 3 B+ single board computer to store the video footage and a wireless endoscope camera that was streaming the video footage wirelessly to a smartphone. The rationale under these two selections is that the first camera setup allows for a fully-customizable means that can support further robotics and automation integration. The second camera (a low-cost commercially-available endoscope) can serve as an off-the-shelf solution to make the work herein self-contained as an intuitive and low-cost way to stream and assess the video footage by the user in a standalone device fashion. Both cameras (one at a time) were mounted onto the chambers via a custom-made 3D printed carbon fiber reinforced mount, which attaches directly on top of the chambers' point of loading the stem of the cut leaf (Fig. 11). The assembly can be removed between measurements and facilitates focal and aperture adjustments to produce clear images of stem samples.

We followed the proper protocol when performing SWP analysis and data acquisition. Sampling was performed mid-day (12PM - 3PM) as per recommendations from relevant literature [5], and leaf samples were bagged with reflective foil bags for at least ten minutes before excision to mitigate water loss through transpiration. During the first session, the excised leaves were placed in an opaque, ice box storage container (not touching the ice) and transported back to the lab for SWP analysis. While earlier literature was recommending making the measurements on the spot and avoid transportation of samples, the work of [14] suggested immediate storage of excised leaf samples in a cold and moist environment helps stabilize the sample's water potential and preserve the condition for hours or even days, depending on the plant species [14]. We followed the standard SWP analysis procedures and proper protocol for sample collection and storage to ensure our image dataset is representative of the real-world underlying conditions. However, in an effort to gather a dataset with more variability to enable more thorough evaluation of our method, in the second session we processed the excised leaves on the spot in the field.

2) **Dataset Creation:** The developed image dataset used for network training, testing and validation consists of 10713 images of dry and wet excised leaf stem cross sections from avocado and orange trees, with a binary class partition of 50.6% dry and 49.4% wet. These images are video frames extracted from our recordings of SWP analysis with the conventional pressure chamber method using all four different setups (recall we used two different pressure chambers and two different miniature cameras). Considering we also use leaves from two distinct tree species, the overall dataset contains images from eight distinctive real-world cases. The majority of the images at this stage, however, are taken from setups involving the static 600D pressure chamber model.

As with any image dataset, the frames were first pre-processed. The video recordings from the Raspberry Pi were first imported to a desktop and converted from h264 to MP4 format. The video resolution was redefined from 1920x1080 to 640x640 (footage was resized to maintain true aspect), to match the expected input image size for the YOLO networks [13] we employed in our learning-based machine vision approach. Videos from the endoscope camera were already of a uniform aspect ratio, so a quick resize from 720x720 to 640x640 was applied to all videos from this setup. Once the video resolutions were redefined, we extracted video frames of interest as images and saved them in the working directory. Finally, all images in the working directory were manually annotated with an open-source YOLO format annotation tool.[7] The resulting labels and frames were then compiled into our stem image dataset with a partition of 7759 training, 1952 validation, and 1002 testing images.

A similar procedure was also performed for the second session which contained images sampled from 20 video instances from leaves excised by lemon and grapefruit trees (10 from each species). In this setting we used one setup, i.e. the pump-up chamber with the high quality Picamera, and conducted measurements in the field under variable ambient light conditions. For this dataset part we extracted and evaluated a total of 45000 images and manually classified them based on xylem wetness status (dry/wet). This dataset part was not used in training, testing, and validation at all. Instead it was used as a way to test the preliminary feasibility of our method to generalize to very diverse out-of-sample cases. In subsection IV-B that follows we employ the first dataset part, whereas subsection IV-C considers the second dataset part.

B. Object Detection of Dry over Wet Stem Condition

YOLO (You Only Look Once) is a single-stage detector capable of performing both object identification and classification in a single shot allowing the network to be smaller and faster [13]. Since its original release, the YOLO family of models has continued to evolve and improve in terms of

---

[6] For more details about these chambers please see the manufacturer's manuals at https://www.pmsinstrument.com/.

[7] For details on the Yolo Annotation Tool please see https://github.com/ManivannanMurugavel/Yolo-Annotation-Tool-New-.

TABLE IV: The three distinctive YOLO networks and variations considered in this work, and training results on our developed stem image dataset with base and tuned hyperparameters and augmentations.

Network	Size (MB)	Training Time (hrs)	Epochs	Recall	Precision	mAP@0.5	mAP@0.5:0.95
YOLOv5 Base	13.8	2.1	80	0.999	1.0	0.995	0.929
YOLOv6 Base	36.3	6.1	80	0.940	0.995	0.995	0.910
YOLOv7 Base	71.4	10.0	80	0.999	1.0	0.998	0.910
YOLOv5 Tuned	13.8	2.4	80	0.999	0.995	0.995	0.885
YOLOv6 Tuned	36.3	6.6	80	0.910	0.995	0.995	0.881
YOLOv7 Tuned	71.4	10.0	80	0.999	0.994	0.998	0.884

structure and performance. In this work, we focused on three YOLO iterations: YOLOv5, YOLOv6, and YOLOv7.[8]

Each network structure consists of 3 main parts: backbone, neck, and head. The YOLOV5 backbone is based on a cross-stage partial network (CSP) [23] to reduce the amount of calculation and increase the speed of inference, and spatial pyramid pooling structure (SPP) [7] to help improve detection accuracy. The adaptive anchor frame calculation on the input image enables automatic setting of the initial anchor frame size and adapting to dataset changes. The neck includes feature pyramid structures of PANet [12] that aim to strengthen the feature extracted from the backbone and further improve the detection capability. The head predicts targets of different sizes based on the obtained feature maps.

The following version, YOLOv6, introduces EfficientRep Backbone and Rep-PAN Neck by replacing the CSP-Block used previously with RepBlock [4]. The new structure has a decoupled head which adds layers separating the features from the final head and has been found able to increase performance. It uses an anchor-free paradigm and SimOTA, a simplified version of OTA (Optimal Transport Assignment) [6] to enhance training speed and detection accuracy.

In the YOLOv7 version, several changes and enhancements were made. Notably, extended efficient layer aggregation networks (E-ELAN) [22] serve as the backbone to improve the learning ability. Compared to the original architecture ELAN, E-ELAN only changes the architecture in computational block as the architecture of transition layer is unchanged. The authors in [22] proposed a new compound scaling method to employ parameters and computation more efficiently and planned a re-parameterized model that can optimize the scaling process and can be applied to concatenation-based models. The head consists of an auxiliary, a lead head, and a soft label assigner for coarse and fine labels.

The efficacy of the trained models was evaluated in terms of three criteria: 1) localize accurately the stem in an image, 2) perform classification of the two states DRY and WET, and 3) have a stable transition from DRY to WET in a video setting.

1) **Network Training Parameters:** Since the three YOLO networks employ distinctive structures, we trained each version from scratch on 7759 training images in two ways: baseline and tuned. The baseline variation features the baseline hyperparameters provided by the developers of the methods in their respective repositories. In the tuned variation, we performed tuning of selected hyperparameters to assess the impact of different data augmentations on each model's performance and training time. Tuned hyperparameters include a decrease in saturation augmentations ($\downarrow$ 0.3 probability), an introduction of rotation augmentations ($\pm$ 45°), and a deletion of the mixup and paste-in augmentations. The baseline hyperparameters feature more emphasis on color space augmentations and less on spatial-level transformations, whereas our tuned hyperparameters emphasize more on spatial-level transformations and less on color space augmentations. We justify our tuning choices by reiterating the findings of [18], where color is not an invariant feature in wetness detection. By training a model on more spatial-level and less color augmentations, we enforce the model to be more sensitive to color space discriminant features and less sensitive to shapes since every sample is unique. All models were trained on a Tesla P100 GPU for 80 epochs, with an initial learning rate of 0.01. For optimization, an SGD optimizer was applied with a momentum of 0.937 and a weight-decay of 0.0005.

2) **Evaluation of Networks' Inference Capabilities***:* We evaluated each trained network on the basis of test classification accuracy, mean average precision, and inference speed. Inference was performed on both cloud and edge computing hardware with test images, and on edge computing hardware with a test video. Table IV presents the training results of all YOLO models with their baseline and tuned hyperparameter variants. Both the baseline and tuned YOLOv5 models achieved the highest mAP@0.5:0.95 scores within their corresponding variants. This means both YOLOv5 models predicted accurately and with high confidence ($\approx$ 0.95) on their detection. Out of all models trained, the tuned YOLOv7 scored the highest mAP@0.5 score, indicating its ability to detect stems close to their ground truth bounding boxes.

Regarding the models' cloud-based inference, we can observe from Table V that our tuning of hyperparameters and augmentations increased the classification performances of YOLOv5 and YOLOv7. Additionally, the inference speed increases marginally for both models. Conversely, YOLOv6 degraded in both classification performance and inference speed under our tuning parameters. Our results for cloud-based inference using a Tesla P100 GPU yielded inference speeds within approximately 30 ms per frame ($\geq$30 FPS), and thus proves real-time water detection with our approach is possible, given equivalent or more powerful computing hardware.

With respect to edge-based inference, and with reference to Table VI, both YOLOv5 models are able to perform predictions within every half second on the NVIDIA Jetson Xavier

---

[8] We wish to highlight here that other learning-based machine vision methods are in principle applicable. However, we elected to work with YOLO in this work due to its widespread use and solid outcomes in a number of distinctive applications. As we show shortly, this method can help reach very high classification accuracy which was deemed sufficient in this work.

NX, and both models also attained a 100% classification accuracy metric on the test images. We observe that all other models attained high classification metrics as well, with the tuned YOLOv7, in particular, scoring a 100% success rate on the test images. Yet, given it is five times larger than YOLOv5, its inference speed was about five times slower than that of the YOLOv5 model, making it less practical for deployment on less powerful edge devices. YOLOv6 experienced a slight inference speed performance boost with our tuning parameters.

TABLE V: Cloud-based inference results with a Tesla P100 on the image test set.

Network	Execution Time (s)	Average Inference Speed per Image (ms)	Classification Accuracy
YOLOv5 Base	27.2	10.4	99.3%
YOLOv6 Base	25.0	25.5	99.5%
YOLOv7 Base	38.1	21.5	99.7%
YOLOv5 Tuned	26.5	8.8	100%
YOLOv6 Tuned	30.0	30.1	99.4%
YOLOv7 Tuned	37.6	21.4	100%

TABLE VI: Edge-based inference results with a Jetson Xavier NX on the image test set.

Network	Execution Time (min)	Average Inference Speed per Image (ms)	Classification Accuracy
YOLOv5 Base	8.04	481.6	100%
YOLOv6 Base	19.57	1171.7	99.5%
YOLOv7 Base	38.69	2316.5	99.7%
YOLOv5 Tuned	7.49	448.4	100%
YOLOv6 Tuned	17.35	1038.9	99.4%
YOLOv7 Tuned	46.24	2769.0	100%

TABLE VII: Edge-based inference results with Jetson Xavier NX on the test video.

Network	Average Inference Speed per Frame (ms)	Stable State Transition
YOLOv5 Base	471.4	No
YOLOv6 Base	1020.0	Yes
YOLOv7 Base	2863.3	Yes
YOLOv5 Tuned	568.1	Yes
YOLOv6 Tuned	1030.9	Yes
YOLOv7 Tuned	2811.6	Yes

Regarding image inference speed, Tables V and VI indicate a direct relation between model size and inference speed. Smaller models tend to perform faster and are thus suited for deployment on devices with limited computational power. Table VII contains the average edge device inference speed results for each model on a test video taken from the dataset preprocessing phase earlier in this work. Similarly to the image inference results, smaller models have faster video inference speeds. As expected, the average inference speed per frame for each model resembles the corresponding metric in edge-based image inference (Table VI).

3) **Qualitative Analysis***:* Figure 12 juxtaposes the wetness detection results on a single orange sample test case by all YOLO models trained on our dataset. Detection confidence is approximately 0.95 and it remains consistent with the bulk of our test results. Comparing the baseline and tuned versions of each model, we can observe that the bounding boxes are slightly tighter around the stem detection for the baseline networks compared to their tuned counterparts. One possible explanation is that the combination of the rotation augmentation and training samples with oversized bounding boxes may have led to removing less amount of the background. As a result, the tuned models have a higher propensity for fitting slightly looser bounding boxes.

When inference is executed at a low confidence threshold (i.e. 0.1), some of the models may occasionally raise a false detection in some of the test cases. Figure 13 shows two illustrative examples of falsely detected instances of dry and wet classes by the baseline YOLOv7. The falsely detected dry case is of only a 0.13 confidence score and can hence be filtered out by specifying a higher confidence threshold of 0.6 as implemented during the evaluation phase. This detection occurred most likely because of some of the training instances featuring a dryer and more heavily brown-colored pith. The reflected light from the chamber lid interface does remotely resemble some of the features present in the aforementioned training instance, but its effects are negligible since the model detected with a low confidence rather than a high confidence (this would have been concerning). In contrast, the false wet detection occurred most likely because of the model recognizing the smooth side of the petiole as wet. The wet confidence score is 0.12.[9] This case emphasizes the importance of aligning the stem sample properly with the camera, as the models may be sensitive to misalignment.

In Table VII, the rightmost column refers to the quality of classification during the video's transitional frames where the state of the stem sample changes from dry to wet. The transitional frames are not considered wet, even with the onset of moisture, because proper SWP analysis protocol defines the wet point as full water expression, whether that be a full clear water drop or a water drop with vigorous bubbling. This helps enforce consistency with SWP measurements. We observed that the tuned models can reach the final WET state more smoothly through the transition phase compared to baseline models. Most notably in the tuned variants of YOLOv6 and YOLOv7, there is minimal classification oscillation during the transitional phase as both models classify consistently dry, until full water expression, when they both classify consistently wet after a brief lull in classification accuracy.

C. Preliminary Evaluation of Generalization Capacity

To assess the generalization capabilities of the proposed models, we further tested the six trained networks on the never-seen-before second dataset part. Note that this dataset part is significantly more challenging because of ambient light variations and large oscillations observed while operating manually the pump-up chamber. Figure 14 highlights some of these challenging instances.

The extracted images were used to evaluate the precision and recall for each model. Obtained results are reported in

---

[9] Its view in the figure is obstructed by the dry bounding box since we increased the line width and font size for inference to improve visibility.

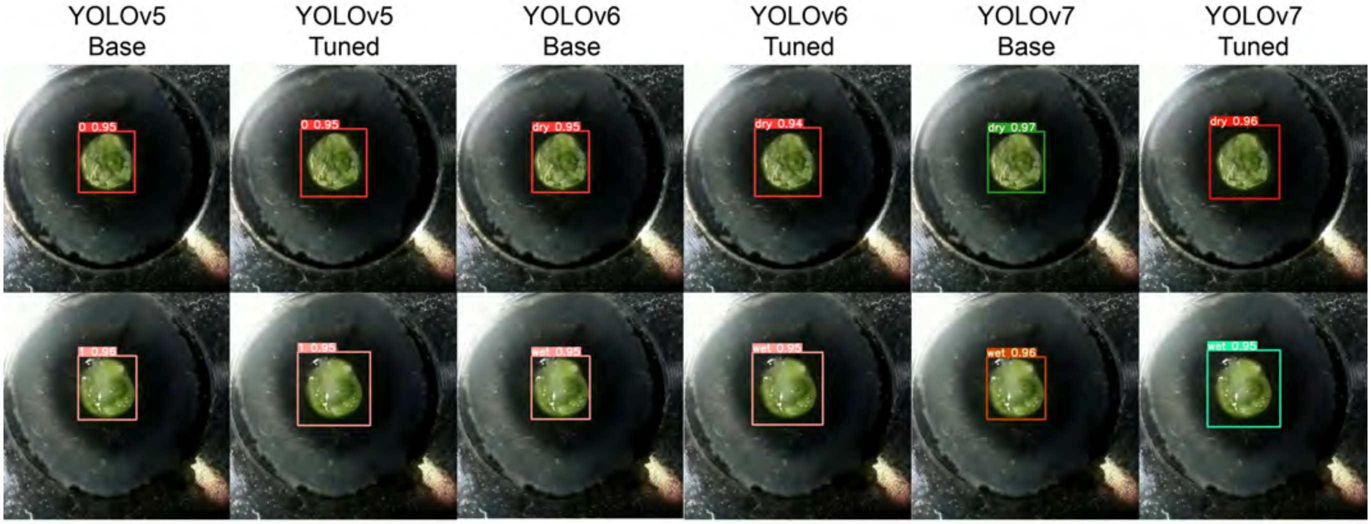

Fig. 12: Correct wetness detection results on a single orange stem by all YOLO models. Top row panels correspond to dry status while bottom row panels to wet status.

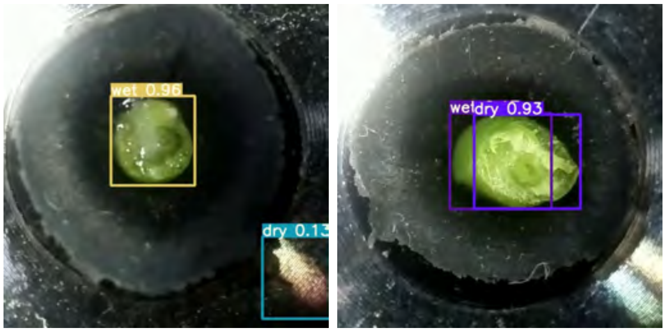

Fig. 13: (Left) Falsely detected dry instance by YOLOv7 base. (Right) Falsely detected wet instance by YOLOv7 base.

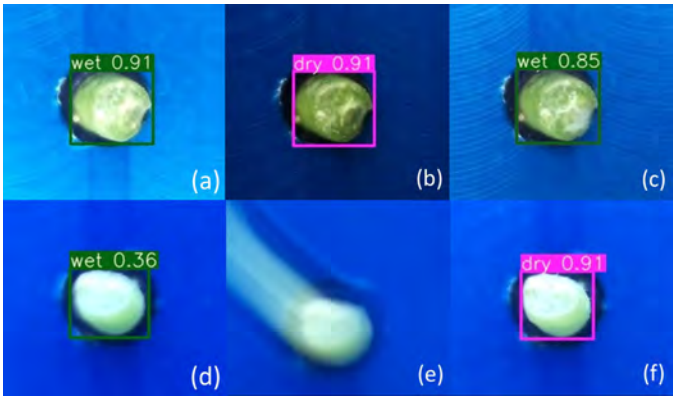

Fig. 14: Examples of how ambient light variation and motion of the pump-up chamber can impact the dataset. Top panels: (a)-(c) Effect of ambient light changes on the xylem state as it evolves from WET in (a) to DRY in (b) and returns to a WET state in (c)–true classification is DRY in (a)-(b) and WET in (c). Bottom panels: (d)-(f) Motion effects impact the detection of the stem in addition to resulting in classification shifts in xylem wetness state: WET in (d) to a no detection in (e) and then DRY in (f)–in all cases true classification is WET.

Table VIII (first six entries in the table). It can be observed that the baseline structures were less efficient as suggested by their precision and recall scores compared to their tuned counterparts. The only exception is the YOLOv5 models which offered the same performance, with a precision of 0.39 and a recall of 0.34. The tuned YOLOv7 network had the highest performance, with a precision score of 0.75 and a recall score of 0.49. A recurring classification error across all networks was the detection of a DRY state as a WET state. This can be attributed to the ambient light variations and motion of the pump-up pressure chamber throughout the analysis, resulting in blurred or distorted images as shown in Fig. 14. However, and in spite of those incorrect state detections, all of the networks were able to properly detect the stem; this feature can be exploited to facilitate network fine-tuning with additional datasets, such as the second dataset part considered herein.

TABLE VIII: Inference results on the dataset evaluating generalization capacity.

Network	Precision	Recall
YOLOv5 Base	0.38	0.34
YOLOv6 Base	0.43	0.32
YOLOv7 Base	0.59	0.47
YOLOv5 Tuned	0.38	0.34
YOLOv6 Tuned	0.56	0.35
YOLOv7 Tuned	0.75	0.49
YOLOv7 Fine-tuned	0.98	0.57

In an effort to assess the effect of fine-tuning on network performance, we retrained the tuned YOLOv7 network using a small sample of the newly obtained data; that is, 1180 images with a ratio of 50% for each wet/dry state. Owing to the fact of training on a small dataset, the model was trained on a Tesla P100 GPU for only 30 epochs at an initial learning rate of 0.01. An SGD optimizer with a momentum of 0.937 and a weight-decay of 0.0005 was used for optimization. Obtained results (last entry of Table VIII) demonstrate a considerable improvement in detection since the accuracy increased from 0.75 to 0.98, suggesting that the structure can now detect the stem in difficult scenarios. The recall increased modestly to 0.57, yet the fine-tuned network was able to provide over 50% more accurate detections. These results demonstrate that more extended fine-tuning, but not a full network retraining, may in fact be sufficient for the methods developed herein to generalize to other tree crop species as well; extending this dataset is part of ongoing work.

V. DISCUSSION AND OUTLOOK

Contributions and Key Findings: In this work, we have presented what, to the best of our knowledge, is the first robot-assisted system for stem water potential (SWP) measurements. The value of this system lies in its capability to autonomously collect samples at scale by automating time-consuming (e.g., leaf collection) or error-prone processes (e.g., identification of the status of the leaf xylem). These are core building-blocks toward enabling complete robot autonomy in physical specimen sampling and transport in the field.

Notably, accurate SWP measurement is instrumental to implement precision agriculture practices to conserve water. Our work demonstrated how it is possible to employ learning-based machine vision to help determine the dry/wet status of the xylem. Results from testing with the static benchtop pressure chamber demonstrated that we can provide stable, crisp, and high resolution and high refresh rate video feed that is annotated in real-time and auto-determines the wetness status of the xylem. This alone can be a major aid to reduce false positive xylem status determination as well as human errors and reading variability when compared to the manual, "look-through-the-hole" approach that is currently the only way to manually observe the wetness status of the xylem. Further, we believe that the produced datasets can stimulate further research on robotics, machine perception, and agronomy, but in addition, lend themselves as a tool to help train human operators in determining stem water potential via the pressure chamber method.

Directions for Future Work: The project outcomes achieved thus far enable various opportunities for future work.

One key direction involves enhancing the detection of xylem water expression by giving heavier consideration to smoothing the transitional phase. Further, we seek to extend the dataset and evaluate the models' performance in other tree crops such as olive and almond trees. Preliminary findings from evaluating the generalization capacity indicated that fine-tuning the networks, or fully retraining with additional data can help expand the method to other tree crops. Two critical factors affecting generalization capacity (especially when using the manual pump-up chamber) are ambient light variations and induced motion. The former can be addressed by possibly adding a cover around the exposed stem. The latter is a challenge inherent to the pump-up chamber, which operates by manual upward/downward strokes (like a pump), but image stabilization techniques can be employed. Nonetheless, we would recommend the use of the static benchtop chamber if possible (at the expense of higher cost to acquire and operate) since it can lead to consistent and high-quality footage.

During the leaf-cutting experiments, we observed that some successful cuts were not accurate enough to be used for SWP analysis (i.e. leaving long-enough stem length to be able to secure the leaf into the pressure chamber's gasket). One main issue was that the front face of the end-effector may push other interconnected leaves and/or branches away, hence the linear approach may not always suffice. Ongoing work aims to improve the end-effector design to a more minimal assembly, and in addition, enhance the perception capabilities of the end-effector to determine when the stem is aligned with the cutting plane to trigger the cutting action. Also relevant is to extend the vision pipeline to determine and localize leaves bagged into reflective foil bags (which allows leaves collected in stem water potential analysis to reach an internal equilibrium thus providing more accurate information regarding the whole tree's water stress).

Another aspect worth exploring is whether it is possible to mount the pressure chamber directly on the robot, to eliminate the need for manual insertion of the leaves into the pressurized chamber. The main challenge to achieve this functionality is in manipulating the stem without compromising its integrity for assessing the leaf xylem.

Finally, more extensive in-field experimentation is needed to test the validity of the system integration we have developed so far. One critical aspect is to further vet these developed tools by growers and agronomists, who can further assess advantages and limitations of the robotic means to estimate crops' needs for watering we have developed so far.

REFERENCES

[1] D. Bochtis, L. Benos, M. Lampridi, V. Marinoudi, S. Pearson, and C.G. Sørensen. Agricultural workforce crisis in light of the covid-19 pandemic. *Sustainability*, 12(19), 2020.

[2] L. Booth and S. Carpin. Distributed estimation of scalar fields with implicit coordination. In *Proceedings of the 16th International Symposium on Distributed Autonomous Robotic Systems*, 2022.

[3] M. Campbell, A. Dechemi, and K. Karydis. An integrated actuation-perception framework for robotic leaf retrieval: Detection, localization, and cutting. In *Proceedings of the IEEE/RSJ International Conference on Intelligent Robots and Systems (IROS)*, pages 9210–9216, 2022.

[4] Y. Chu et al. Yolov6: A fast and accurate, open source target detection framework. Technical report, Meituan Technical Team, 2022.

[5] A. Fulton, J. Grant, R. Buchner, and J. Connell. Using the pressure chamber for irrigation management in walnut, almond and prune. *ANR*, 2014.

[6] Z. Ge, S. Liu, Z. Li, O. Yoshie, and J. Sun. Ota: Optimal transport assignment for object detection. In *Proceedings of the IEEE/CVF Conference on Computer Vision and Pattern Recognition (CVPR)*, pages 303–312, 2021.

[7] K. He, X. Zhang, S. Ren, and J. Sun. Spatial pyramid pooling in deep convolutional networks for visual recognition. *IEEE Transactions on Pattern Analysis and Machine Intelligence*, 37(9):1904–1916, 2015.

[8] J.R. Jankowski. *Consumptive Water Use in California's Sacramento-San Joaquin Delta: A Comparison of Estimation Methods and Field Data, with Implications for Water Right Diversion Reporting*. University of California, Davis, 2018.

[9] X. Kan, H. Teng, and K. Karydis. Multi-robot field exploration in hex-decomposed environments for dubins vehicles. In *Proceedings of the IEEE International Conference on Robotics and Biomimetics (ROBIO)*, pages 449–455, 2019.

[10] X. Kan, H. Teng, and K. Karydis. Online exploration and coverage planning in unknown obstacle-cluttered environments. *IEEE Robotics and Automation Letters*, 5(4):5969–5976, 2020.

[11] X. Kan, T. Thayer, S. Carpin, and K. Karydis. Task planning on stochastic aisle graphs for precision agriculture. *IEEE Robotics and Automation Letters*, 6(2):3287 – 3294, 2021.

[12] S. Liu, Lu Qi, H. Qin, J. Shi, and J. Jia. Path aggregation network for instance segmentation. In *Proceedings of the IEEE/CVF Conference on Computer Vision and Pattern Recognition (CVPR)*, pages 8759–8768, 2018.

[13] J. Redmon, S. Divvala, R. Girshick, and A. Farhadi. You only look once: Unified, real-time object detection. In *Proceedings of the IEEE/CVF Conference on Computer Vision and Pattern Recognition (CVPR)*, pages 779–788, 2016.

[14] C. M. Rodriguez-Dominguez, A. Forner, S. Martorell, et al. Leaf water potential measurements using the pressure chamber: Synthetic testing of assumptions towards best practices for precision and accuracy. *Plant, Cell & Environment*, 45(7):2037–2061, 2022.

[15] G. D. Schaible and M. P. Aillery. Water conservation in irrigated agriculture: Trends and challenges in the face of emerging demands. Technical Report EIB-99, U.S. Department of Agriculture, Economic Research Service, September 2012.

[16] P. F. Scholander, H. T. Hammel, E. A. Hemmingsen, and E. D. Bradstreet. Hydrostatic pressure and osmotic potential in leaves of mangroves and some other plants. *Proceedings of the National Academy of Sciences of the United States of America*, 52(1):119, 1964.

[17] A. Shamshirgaran and S. Carpin. Reconstructing a spatial field with an autonomous robot under a budget constraint. In *Proceedings of the IEEE/RSJ International Conference on Intelligent Robots and Systems (IROS)*, pages 8963–8970, 2022.

[18] A. Swarup, W. S. Lee, N. Peres, et al. Strawberry plant wetness detection using color and thermal imaging. *Journal of Biosystems Engineering*, 45:409–421, 2020.

[19] G. Vellidis, V. Liakos, W. Porter, M. Tucker, and X. Liang. A dynamic variable rate irrigation control system. In *Proceedings of the International Conference on Precision Agriculture*, volume 13, pages 1–9, 2016.

[20] H Vila, I Hugalde, and M Di Filippo. Estimation of leaf water potential by thermographic and spectral measurements in grapevine. *RIA: Revista de Investigaciones Agropecuarias*, 37:46–52, 2011.

[21] J.S. Wallace and P.J. Gregory. Water resources and their use in food production systems. *Aquatic Sciences*, 64:363–375, 2002.

[22] C. Wang, A. Bochkovskiy, and H. M. Liao. YOLOv7: Trainable bag-of-freebies sets new state-of-the-art for real-time object detectors. *arXiv preprint arXiv:2207.02696*, 2022.

[23] C. Wang, Hong-Yuan M. L., Y. Wu, et al. Cspnet: A new backbone that can enhance learning capability of cnn. In *Proceedings of the IEEE/CVF Conference on Computer Vision and Pattern Recognition (CVPR) Workshops*, pages 1571–1580, 2020.

[24] S. Wang, L. Ren, Y. Liu, Z. Han, and Y. Yang. Mechanical characteristics of typical plant leaves. *Journal of Bionic Engineering*, 7(3):294–300, 2010.

[25] T. Zhao, B. Stark, Y. Chen, A.L. Ray, and D. Doll. Challenges in water stress quantification using small unmanned aerial system (suas): Lessons from a growing season of almond. *Journal of Intelligent & Robotic Systems*, 88(2):721–735, 2017.

[26] Q. Zhou, J. Park, and V. Koltun. Open3D: A modern library for 3D data processing. *arXiv:1801.09847*, 2018.